Neodymium isotopic constraints on Cenozoic Asian dust provenance changes linked to the exhumation history of the northern Tibetan Plateau and the Central Asian Orogenic Belt

Yibo Yang, Albert Galy, Xiaomin Fang, Rongsheng Yang, Wenfang Zhang, Bowen Song, Yudong Liu, Wenxia Han, Weilin Zhang, Song Yang

To cite this version:

Yibo Yang, Albert Galy, Xiaomin Fang, Rongsheng Yang, Wenfang Zhang, et al.. Neodymium isotopic constraints on Cenozoic Asian dust provenance changes linked to the exhumation history of the northern Tibetan Plateau and the Central Asian Orogenic Belt. Geochimica et Cosmochimica Acta, 2021, 296, pp.38-55. ⟨10.1016/j.gca.2020.12.026⟩. ⟨hal-03401628⟩

HAL Id: hal-03401628
https://hal.science/hal-03401628v1

Submitted on 12 May 2023

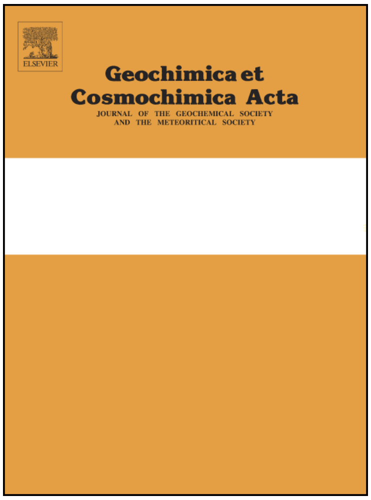

Neodymium isotopic constraints on Cenozoic Asian dust provenance changes linked to the exhumation history of the northern Tibetan Plateau and the Central Asian Orogenic Belt

Yibo Yang, Albert Galy, Xiaomin Fang, Rongsheng Yang, Wenfang Zhang, Bowen Song, Yudong Liu, Wenxia Han, Weilin Zhang, Song Yang

PII: S0016-7037(20)30739-0
DOI: https://doi.org/10.1016/j.gca.2020.12.026
Reference: GCA 12027

To appear in: *Geochimica et Cosmochimica Acta*

Received Date: 15 June 2020
Revised Date: 22 December 2020
Accepted Date: 29 December 2020

Please cite this article as: Yang, Y., Galy, A., Fang, X., Yang, R., Zhang, W., Song, B., Liu, Y., Han, W., Zhang, W., Yang, S., Neodymium isotopic constraints on Cenozoic Asian dust provenance changes linked to the exhumation history of the northern Tibetan Plateau and the Central Asian Orogenic Belt, *Geochimica et Cosmochimica Acta* (2021), doi: https://doi.org/10.1016/j.gca.2020.12.026

Neodymium isotopic constraints on Cenozoic Asian dust provenance changes linked to the exhumation history of the northern Tibetan Plateau and the Central Asian Orogenic Belt

Yibo Yang[1,2*], Albert Galy[3], Xiaomin Fang[1,2,4*], Rongsheng Yang[2,3,4], Wenfang Zhang[5], Bowen Song[6], Yudong Liu[2,4], Wenxia Han[7], Weilin Zhang[1,2], and Song Yang[8]

[1] CAS Center for Excellence in Tibetan Plateau Earth Sciences, Chinese Academy of Sciences, Beijing, China

[2] Key Laboratory of Continental Collision and Plateau Uplift, Institute of Tibetan Plateau Research, Chinese Academy of Sciences, Beijing, China

[3] Centre de Recherches Pétrographiques et Géochimiques, UMR7358, CNRS, Université de Lorraine, Nancy, France

[4] University of Chinese Academy of Sciences, Beijing, China

[5] State Key Laboratory of Lake Science and Environment, Nanjing Institute of Geography and Limnology, Chinese Academy of Sciences, Nanjing, China

[6] Institute of Geological Survey, China University of Geosciences, Wuhan, China

[7] Shandong Provincial Key Laboratory of Water and Soil Conservation and Environmental Protection, College of Resources and Environment Sciences, Linyi University, Linyi, China

[8] Key Laboratory of Tibetan Environment Changes and Land Surface Processes, Institute of Tibetan Plateau Research, Chinese Academy of Sciences, Beijing, China

*Corresponding author: Y. Yang (yangyibo@itpcas.ac.cn) and X. Fang (fangxm@itpcas.ac.cn)

Abstract

The arid interior of Asia is the largest source of dust deposited in the North Pacific Ocean, and some dust is even transported to Greenland. Investigating the provenance history of Asian dust can provide strong constraints on the evolution of topography and climate in the Asian interior. Eolian dust Nd isotopic records preserved in North Pacific Ocean sediments since ~40 Ma provide a spatially integrated first-order constraint on the provenance changes of Asian dust. However, a lack of similarly long dust Nd isotopic records from Asian dust source areas, namely, the northern Tibetan Plateau and the Central Asian Orogenic Belt, has hindered a full understanding of Asian dust provenance changes linked to the Cenozoic evolution of tectonics, climate and topography in inland Asia. Here, we have constructed the first fine-grained and whole-rock Nd isotopic records from sediments deposited on the northern Tibetan Plateau since ~ 52 Ma. The results indicate two major changes, a gradual increase in $\varepsilon_{Nd}(0)$ values between ~42 Ma and ~25 Ma and a general decrease since ~25 Ma, which were probably caused by the incremental northward growth of the Tibetan Plateau. Further mass balance estimates based on comparisons between the Nd isotopic characteristics of dust from the northern Tibetan Plateau and the North Pacific Ocean indicate that a rapid increase in the contribution of the Central Asian Orogenic Belt to Asian dust at ~25 Ma can be closely linked to rapid exhumation caused by tectonic uplift and aridification in inland Asia. Our provenance analyses, together with the onset of eolian sediment in central and eastern Asia, suggest that a modern-like regime promoting Asian dust emissions and transport might have been in place since the late Oligocene.

1 INTRODUCTION

As the largest temperate arid region, inland Asia delivers the second largest amount of eolian dust to regions downwind. Dust accumulation in downwind eastern Asia has formed thick eolian sequences in the Chinese Loess Plateau (CLP) since the late Oligocene (Guo et al., 2002; Qiang et al., 2011), and significant quantities of dust have also been transported many thousands of kilometers to the Japan Sea, the North Pacific Ocean (NPO) and even Greenland (e.g., Rea et al., 1998). Asian dust deposition is an excellent archive of Cenozoic changes in climate, erosion, and atmospheric circulation in the Asian interior. Asian dust source areas can be divided into two regions with different geological properties and compositions (Che and Li, 2013; Chen et al., 2007; Li et al, 2009, 2011; Nakano et al., 2004, Zhao et al., 2014, 2015). In particular, the northern Tibetan Plateau (NTP) is characterized by very negative sediment $\varepsilon_{Nd}(0)$ values (with a mean $\varepsilon_{Nd}(0)$ value of surface sediments of -12.3), while the Central Asian Orogenic Belt (CAOB) features less negative sediment $\varepsilon_{Nd}(0)$ values (with a mean $\varepsilon_{Nd}(0)$ value of surface sediments of -4.4) (e.g., Li et al., 2011). In more detail (Table S1), previously reported Nd isotopic data for various surface soil and sediment samples across northern China and Mongolia have shown that the CAOB region along the northern boundary of China and southern Mongolian Gobi is generally characterized by high $\varepsilon_{Nd}(0)$ values that are mostly >-6, the Qilian Shan region features very low $\varepsilon_{Nd}(0)$ values of approximately -12, and the Erdos region features the lowest $\varepsilon_{Nd}(0)$ values of <13 (Blayney et al., 2019; Chang et al., 2000; Chen et al., 2007; Clift et al., 2017; Garzione et al., 2005; He et al., 2019; Li et al., 2009; Liu et al., 1994; Nakano et al., 2004; Rao et al., 2015; Wu et al., 2010; Zhao et al., 2014, 2015). Investigating the provenance history of Asian dust can place a strong constraint on the evolution of topography and climate in the Asian interior. In the NPO, core LL44-GPC3 (hereafter GPC3) has provided the most complete and spatially integrated Asian dust record since ~40 Ma using Nd isotopes as tracers of eolian dust sources (Pettke et al., 2002a). However, the lack of corresponding dust Nd isotopic records in the NTP and/or CAOB regions since at least 40 Ma prevents a full interpretation of the GPC3 record in terms of the respective roles of tectonic uplift and climatic drying and the locations of those processes.

To date, the long-term Cenozoic Nd isotopic variation history in the CAOB region has never been reported. A few Nd isotopic records from the NTP region have been reported in the Linxia Basin (Garzione et al., 2005; Yang et al., 2017), the Xining Basin (He et al., 2019) and the Tarim Basin (Blayney et al., 2019). These Cenozoic Nd isotopic records in the NTP region have only been used to interpret basin-wide provenance changes, and their use for the investigation of the provenance history of Asian dust requires some cautious interpretation and synthesis. Therefore, first, the collection and addition of new data to the existing records will allow a better and broader regional scale quantification of an overall continuous record of Nd isotopic variation for the entire NTP region. In this sense, a mass balance approach of the Cenozoic Nd isotopic evolution of both the NTP region and the NPO region can help to explore Nd isotopic changes in the CAOB region. Second, the existing Nd isotopic records are all from bulk fluvial-lacustrine sediments, but only the very fine fraction represents eolian dust that has been transported thousands of kilometers to the NPO region. Modern investigations have shown that the coarse and fine fractions in dune and fluvial-lacustrine sediments (75-500 μm vs. <75 μm) in the Qaidam Basin (Du et al., 2018) and in desert/river sands (<75 μm vs. <5 μm) in major Chinese deserts (Chen et al., 2007) exhibit Nd isotopic differences as large as 2-3 ε_{Nd} units. Such large differences can also be seen in sand-mud pairs in modern deep-sea turbidites from different tectonic settings (McLennan et al., 1989). Given that the variability across the ~40 Myr Nd isotopic record in the NPO is only ~3 ε_{Nd} units (Pettke et al., 2002a), further work is therefore required to assess the true

Nd isotopic signature of the material potentially contributing to the eolian dust transported to the NPO. Finally, the NTP contribution to Asian eolian dust in the Paleogene is less understood than that in the Neogene. The rapid uplift of the Qilian Shan (Fig. 1) is thought to have played a critical role in the generation and transport of Neogene dust to the NPO and CLP (e.g., Chen and Li, 2013; Li et al., 2011). Considering a model of incremental northward growth of the plateau (e.g., Tapponnier et al., 2001; Law and Aleen, 2020), however, the Qilian Shan might have been less exhumed in the Paleogene than at present. There is a need for a more detailed characterization of the Nd isotopic signature of the terranes that experienced uplift earlier than the Qilian Shan in the NTP, such as the East Kunlun Shan or Songpan-Ganzi terrane (Fig. 1).

Here, we present new Nd isotopic data from modern fluvial sediment samples across the entire Qaidam and Xining Basins on the eastern NTP to distinguish the Nd isotopic characteristics of the Qilian Shan from those of the East Kunlun Shan, Altyn Tagh, and Laji Shan (Fig. 1). When compared with previously reported Nd isotopic data, these new data define a more comprehensive Nd isotopic signature of the NTP region. We also establish an integrated Cenozoic Nd isotopic record of fine material in the NTP region based on previous records and two new Nd isotopic records in the Xining Basin from 52 to 17 Ma and in the Linxia Basin from 23 to 5 Ma using both bulk sediments and clay fractions (<2 μm). Finally, we compare the reconstructed Nd isotopic variation in fine material from the NTP fine material with that from the NPO to further assess the relative contributions of the NTP vs. CAOB to Asian dust and discuss the implications for the exhumation and growth of the mountains in the NTP and CAOB regions.

2. GEOLOGICAL SETTING

The Xining and Linxia Basins lie on the northeastern margin of the Tibetan Plateau and on the western margin of the CLP (Figs. 1a, 1b). Both basins correspond to subbasins of a larger

Paleocene-Miocene basin complex named the Longzhong Basin (Zhai and Cai, 1984; Fig. 1). The Cenozoic boundaries of the exposed Longzhong Basin are the Qilian-Haiyuan faults to the north, the Liupan Shan fault to the east, the Haiyan-Laji Shan-Leiji Shan faults to the west, and the North Qinling fault to the south (Fig. 1b). The Cenozoic stratigraphy of the Longzhong Basin is divided into the Paleogene Xining Group and the Neogene Guide Group (Zhai and Cai, 1984). The Xining Group consists of a lower portion composed of red-orange clastic sediments and an upper portion composed of red mudstone with distinctive intercalations of gypsum deposits. The Guide Group generally consists of light brown to yellow mudstones with intercalated sandy and conglomeratic lenses that are rich in mammal fossils.

The Xining Basin is confined by three NW-SE-trending dextral transpressional faults, and it is surrounded by the Laji Shan, Riyue Shan and Daban Shan mountains to the south, west and north, respectively (Dai et al., 2006; Fig. 1). The Laji Shan is mainly composed of Paleozoic basic to intermediate volcanic, volcaniclastic, and clastic rocks, while the Daban Shan is composed of early Paleozoic marine clastic, volcanic and volcaniclastic rocks (Wang et al., 2015). A >2 km-thick Cenozoic sedimentary succession lies unconformably on Jurassic-Cretaceous terrestrial clastic rocks (Wang et al., 2015; Zhang et al., 2016). Good exposure of the Cenozoic sediments can be found along deeply incised valleys of the Huangshui River and its tributaries (Fig. 1c).

The Linxia Basin, ~200 km to the southeast of the Xining Basin, is surrounded by a series of strike-slip faults, including the Haiyuan-Liupan Shan fault to the north and east and the Laji Shan-Jishi Shan fault to the west (Fig. 1d). The surrounding mountains (the Maxian Shan to the north, West Qinling Mountains to the south and Jishi Shan to the west) mostly consist of Devonian-Permian clastic rocks and carbonates and Mesozoic intermontane red bedrock (Fang et al., 2003). Southwest of the Linxia Basin, the northeastern margin of the Tibetan Plateau consists of rocks of the eastern Kunlun-Qaidam terrane and the Songpan-Ganzi complex (Yin and Harrison, 2000). The Linxia Basin's Cenozoic sediments unconformably overlie Paleozoic Caledonian granitic rocks in the center of the basin and Cretaceous sedimentary rocks in the north of the basin (Fang et al., 2003). The Cenozoic stratigraphy of the Linxia Basin consists mainly of red beds of fluvio-lacustrine mudstones and siltstones in its center and thick strata of gray to reddish-brown conglomerates and sandstones on its margins, and these deposits are often >1 km thick.

3 MATERIALS AND METHODS

Thirty-nine modern/recent fluvial sediment samples from the Qaidam Basin and the Xining Basin and one lake sediment sample from Hala Lake located in the Qilian Shan were collected to assess the differences in the Nd isotopic ratios between the Qilian Shan and the adjacent mountains (Fig. 1). Two suites of bulk and clay-sized sediments were obtained, one from the Xiejia (XJ) section in the Xining Basin and the other from the Heilinding (HLD) section in the Linxia Basin (Fig. 1). A total of 86 bulk (39 modern sediments, 17 from the HLD section, and 30 from the XJ section) and 64 clay-sized samples (30 from the HLD section and 34 from the XJ section) were chosen to measure the ^{143}Nd/^{144}Nd ratios following Yang et al. (2017) in CRPG-CNRS-UL (Nancy, France). Detailed magnetostratigraphy, biostratigraphy and tephrochronology have determined that the HLD section was deposited from 23.3-1.8 Ma (Fang et al. 2016) and that the XJ section was deposited from 52-17 Ma (Dai et al., 2006) (Figs. 2, 3). The HLD composite section consists of borehole HZT (129.2 m) in the upper part, outcrop HLD (226.5 m) in the middle part, and borehole HZ (477.7 m) in the lower part (Fang et al., 2016). Here, we chose samples from the HLD outcrop and HZ borehole, corresponding to ages from 23.3-5.2 Ma (Fig. 2). The studied strata are dominated by mudstones and siltstones interbedded with some layers of sandstones and conglomerates, representing an environment dominated by large river channel facies, floodplain facies, and braided river facies (Fang et al., 2016). The XJ section is dominated by homogeneous fine-grained siltstones and mudstones intercalated with gypsum layers before ca. 33 Ma, representing alternations between dry distal floodplain mudflats and fine-grained siltstones and mudstones after ca. 33 Ma, corresponding to a dominant distal floodplain environment later (Fig. 3).

Clay fractions were obtained using approximately 50 g of bulk sample. To promote clay dispersion, organics and carbonate were removed with excess 25% peroxide followed by 1 M diluted acetic acid. The clay fraction (<2 μm) of the sediments in both sections was separated by gravitational sedimentation following Stokes' law. To avoid possible Nd isotopic differences caused by pretreatment differences, the obtained clay-sized samples and the bulk samples were pretreated with exactly the same procedures described below. In brief, ~100-150 mg of bulk or clay-sized samples were washed twice in 10 ml pure water (18.2 MΩ, Millipore water) to remove water-soluble salts (e.g., gypsum in the XJ section), with each round involving ultrasonic oscillation lasting 2 h and centrifuging at 5000 rpm. This procedure was followed by leaching in 10 ml of 10% (v/v) unbuffered acetic acid solution (Seastar, Plasma pure, distilled twice in the laboratory) twice at room temperature, with each round involving ultrasonic oscillation lasting 30 min and centrifuging at 5000 rpm. The acetic acid leach was used here to remove any carbonates, especially calcite and possible trace dolomite in the saline lake sample from the XJ section. In continental settings, Ca and Mg from noncarbonate phases in carbonate-poor sediments can be released when using 10% unbuffered acetic acid solution (Yang et al. 2016; Ruan et al., 2019). However, we used the identical pretreatment of excess acetic acid for the bulk and clay-sized samples. The bulk sediments generally have less than 20% carbonate. Thus, there was no real difference in the pH of the leaching reaction. In addition, the amount of rare earth elements (REEs) released by the leaching of continental sediments by unbuffered diluted acetic acid has been interpreted to reflect the content of authigenic phases precipitated in river and/or lake settings (Yang et al., 2014). Therefore, any large differences in the Nd isotopic composition of the clay-sized and bulk samples cannot be related to the difference in the amount of authigenic phases between the two types of material but are more likely to reflect a difference in provenance. After acetic acid leaching, the residual material was cleaned three times in ultrapure water, freeze-dried and put into a platinum crucible at 600 °C for at least 4 h to remove any organic matter.

The residual silicate material was then digested by pressurized acid digestion using a mixed HNO_3/HF solution, and Nd was separated using standard techniques (Pin and Zalduegui, 1997) in a clean room of CRPG-CNRS-UL. Rare earth elements were first separated from the bulk sample by cation exchange chromatography using TRU resin (50-100 μm, TrisKem International). The Nd fraction was further isolated from the other light REEs using Ln-spec resin (100-150 μm, TrisKem International). The $^{143}Nd/^{144}Nd$ ratios were measured using a Neptune Plus multicollector inductively coupled plasma mass spectrometer at CRPG-CNRS-UL. The measured $^{143}Nd/^{144}Nd$ ratios were normalized to $^{146}Nd/^{144}Nd = 0.7219$ (Wasserburg et al., 1981) by the exponential law and to the JNdi-1 ratio $^{143}Nd/^{144}Nd = 0.512115$ (Tanaka et al., 2000) by using a true bracketing linear correction following Wilson et al. (2012). Reproducibility was periodically checked by running the Nd standard JNdi-1, which returned an external standard deviation of 0.000009 (2σ, n=81). A total of 56 clay-sized samples from the HLD and XJ sections was digested by pressurized acid digestion using a mixed HNO_3/HF solution (Yang et al., 2015), and the Nd concentrations were measured by an inductively coupled plasma mass spectrometer (X-7; Thermo-Elemental, USA) at the Institute of Tibetan Plateau Research, Chinese Academy of Sciences, Beijing. Relative standard deviations from the mean value of replicate analyses were less than 5%.

4 RESULTS

Nd isotopic compositions are expressed as $\varepsilon_{Nd}(0) = ((^{143}Nd/^{144}Nd)_{sample}/(^{143}Nd/^{144}Nd)_{CHUR} - 1) \times 10^4$, where $(^{143}Nd/^{144}Nd)_{CHUR} = 0.512638$, Jacobsen and Wasserburg, 1980), and together with the Nd concentrations are listed in supplementary Tables S1 and S2. The $\varepsilon_{Nd}(0)$ variations in the HLD and XJ sections (from the Linxia and Xining Basins) are shown in Figures 2 and 3, respectively. In the HLD section, the $\varepsilon_{Nd}(0)$ values range from -8.9 to -10.9 for clay-sized samples and from -9.2 to -11.8 for bulk samples, while those in the XJ section range from -8.5 to -11.4 for clay-sized samples and from -9.0 to -12.4 for bulk samples. There is a statistically significant ($p<0.001$) positive linear correlation between the $\varepsilon_{Nd}(0)$ values of the clay-sized fraction and those of the bulk sample in both sections (Fig. 4). However, the $\varepsilon_{Nd}(0)$ values of the clay-sized fraction are generally higher than the $\varepsilon_{Nd}(0)$ values of the bulk samples (mostly within 1 ε_{Nd} unit except for sediments older than ~42 Ma in the XJ section with a greater offset of 1-2 ε_{Nd} units) in both sections. There are also a few exceptions where the clay-sized $\varepsilon_{Nd}(0)$ values are close to or lower than those of the bulk samples, e.g., samples at 355 m, 462.1 m, 702 m, and 758.1-814.2 m in the XJ section and 826 m and 376 m in the HLD section. The shape of the long-term Nd isotopic variations in the clay-sized fraction is similar to that of the bulk data (Figs. 2, 3). The Nd isotopic values in the Linxia Basin exhibit a general decrease with two obvious decreases at ~15 Ma and ~9-8 Ma, while those in the Xining Basin show a long-term increase from ~ 42 Ma to ~24-26 Ma and a significant decrease since ~24-26 Ma.

5 DISCUSSION

5.1 Modern Nd isotopic distribution in the Asian dust source areas

Bulk and clay-sized (<2 μm) Nd isotopic data from Gobi and sandy deserts in northern China and southern Mongolia confirm a close link between the isotopic compositions of deserts and the tectonic settings of the surrounding mountains (Chen et al., 2007; Zhao et al., 2014). The NTP is characterized by more negative $\varepsilon_{Nd}(0)$ values. With the new data from the eastern portion of the NTP, the modern Nd isotopic distribution in the NTP region shows that the Qilian Shan acts as a source with low $\varepsilon_{Nd}(0)$ values of approximately -12. Furthermore, there are clear isotopic boundaries with the nearby Altyn Tagh and East Kunlun Shan to the west (Figs. 5b, 5c) and the Laji Shan and West Qinling Mountains to the south (Fig. 5d). In more detail, the river sediments from the northern tributaries of the Huangshui River provide a spatial average corresponding to the Daban Shan (southeast termination of the Qilian Shan). Their $\varepsilon_{Nd}(0)$ values, with an average of -11.3 (n=7), are lower than those of the southern tributaries from the Laji Shan (Fig. 5d), at approximately -8.7 (n=4). The ε_{Nd} values <-13 in the surface sediments around Erdos likely indicate the dominance of the North China Craton, which consists of uniformly Archean to Paleoproterozoic basement, as the source of the sediments. The provenance regime, as shown by the $\varepsilon_{Nd}(0)$ values in the NTP region, is best explained by the sequential accretion, from north to south, of several microcontinents and flysch complexes onto the southern margin of the North China Craton-Tarim Block since the early Paleozoic (Yin and Harrison, 2000). The compilation also shows that the West Qinling Mountains near the Linxia and Xining Basins display $\varepsilon_{Nd}(0)$ values between -10 and -13, which are lower than $\varepsilon_{Nd}(0)$ values between -6 and -10 in the Laji Shan, East Kunlun Shan and Songpan-Ganzi terrane (Figs. 5c, 5d). In addition, the western margin of the Tarim Basin (Pamir region) features $\varepsilon_{Nd}(0)$ values of approximately -10, similar to those in the East Kunlun Shan and Songpan-Ganzi terrane but ~1 ε_{Nd} unit higher than those on the southern margin of the Tarim Basin (the West Kunlun and the Altyn Tagh) and in basin interior. The West Kunlun orogenic belt formed through the accretion and collision of magmatic arcs with the Tarim block (Pan et al., 1990, 1996; Xiao et al., 2002). The difference in the Nd isotopic signature of the western Tarim Basin is likely related to the accretion of other terrains by the indentation of the Pamir and associated complex tectonic setting (Chapman et al., 2018; Blayney et al., 2019; Laborde et al., 2019). The higher $\varepsilon_{Nd}(0)$ values of modern fluvial sediment in the western Tarim Basin compared to those in the rest of the basin and basin interior (Fig. 5b) conform to the pattern in which source rocks with high $\varepsilon_{Nd}(0)$ values are distributed only in the NW Tarim Basin and the southern Tian Shan (Clift et al., 2017).

The CAOB, which is characterized by relatively negative $\varepsilon_{Nd}(0)$ values, documents the accretion of island arcs, ophiolites, oceanic islands, seamounts, accretionary wedges, oceanic plateaus and microcontinents from ~1000 to 250 Ma in a manner comparable to that of the circum-Pacific Mesozoic-Cenozoic accretionary orogens (Windley et al., 2007). Thus, the CAOB consists of young dominantly mantle-derived volcanic and plutonic rocks characterized by ε_{Nd} values that are less negative than those of the upper continental crust (e.g., McLennan, 1993). In more detail, the $\varepsilon_{Nd}(0)$ values of clay-sized sediment from the Northern Mongolia Plateau, ranging from -5.1 to -11.5, reflect the contribution from island arcs, accretionary wedges, passive and active margins, and Precambrian microcontinents (Fig. 5; Zhao et al., 2015). However, the more radiogenic values of the Southern Mongolia Gobi from -2.7 to -6.0 (Fig. 5; Zhao et al., 2015) are better explained by contributions from the Silurian, Devonian and Carboniferous accretionary complexes and arc-related volcanic-volcaniclastic rocks (Lamb and Badarch, 1997; Windley et al., 2007). Since the Northern Mongolia Plateau is not a source of the dust transported over long distances to the NPO

(Zhao et al. 2015), we do not include its $\varepsilon_{Nd}(0)$ values in the CAOB dust endmember dataset in the following mass balance estimates.

5.2 Cenozoic Nd isotopic variation in the northern Tibetan Plateau

5.2.1 Linxia Basin

The Nd isotopic records display a general decrease in the values of the bulk and <2 μm samples (Fig. 6a) in the fluvial HLD section on the southern margin of the basin (Fig. 1d), with a maximum variation range of 2.6 ε_{Nd} units for the bulk samples. The records of bulk fluvial-lacustrine sediments from the Maogou (MG) and Wangjiashan (WJS) sections (Garzione et al., 2005) in the center of the Linxia Basin (Fig. 5d) are much more spiky (with a total range of 5.7 ε_{Nd} units) and agree with the HLD bulk rock records only for ages >20 Ma and approximately 10 Ma (Fig. 6a). This discrepancy between the southern margin (HLD section) and the center (MG and WJS sections) of the Linxia Basin could correspond to the contribution of more variable sources of detrital materials in the center of the basin, potentially including contributions from a northern source that do not reach the southern margin. However, high $\varepsilon_{Nd}(0)$ values (>-8) are not present in the eastern termination of the Laji Shan (Fig. 5d). Therefore, the differences between the HLD section (this study) and the MG and WJS sections (Garzione et al., 2005) are difficult to explain by differences in provenance, and the different pretreatments of the samples may have contributed to the distinct Nd isotopic values. The bulk samples in this study were decarbonated by leaching, which also removes almost all the Nd carried by authigenic phases (e.g., Wilson et al., 2013), while those in Garzione et al. (2005) were digested without prior leaching steps. Therefore, the greater variability and higher $\varepsilon_{Nd}(0)$ values in the MG and WJS sections than in the HLD section could correspond to a greater presence of authigenic phases in sediments in the center of the basin than in sediments deposited on its southern margin.

Despite the distinct variability in both records, the long-term decrease in $\varepsilon_{Nd}(0)$ values in the previously described MG and WJS sections and the detrital data from the HLD section suggest a generally consistent evolution of the basin sediments. The variations in the $\varepsilon_{Nd}(0)$ values in the Qin'an section from the nearby Tianshui Basin (Fig. 6a) also display a long-term decrease consistent with records from the Linxia Basin (Fig. 6a). The Qin'an section comprises eolian sediments dominantly from the eastern NTP region (Chen and Li, 2013; Liu et al., 2019). The similar long-term $\varepsilon_{Nd}(0)$ variations between fluvial (Linxia Basin) and eolian (Tianshui Basin) records suggest uniform Neogene $\varepsilon_{Nd}(0)$ variations over the broad source area in the eastern NTP region.

5.2.2 Xining Basin

Two nearby sections, the XG-TS composite section (53-16 Ma, He et al., 2019) and the XJ section in our study (Fig. 5d), show nearly the same variation in the bulk Nd isotopic data, with an increasing trend between ~42 and ~24-26 Ma and a significant decrease since ~24-26 Ma (Fig. 6b). For the younger portion of the records, the decrease in the bulk $\varepsilon_{Nd}(0)$ values in the Xining Basin matches those in the bulk $\varepsilon_{Nd}(0)$ records from the Linxia Basin and the Tianshui Basin, although there could be some significant differences among the records at ~20-25 Ma (Fig. 6b). Consistent trends can also be seen in the clay-sized fraction data from the Xining and Linxia Basins and in the 28-45 μm fraction data from the Tianshui Basin (Fig. 6b). All of the above observations imply that samples from these three basins – Tianshui, Linxia and Xining – can be used to create an integrated record of long-term Cenozoic $\varepsilon_{Nd}(0)$ variations in clastic material and very fine dust in the eastern NTP that can be transported to the NPO.

5.2.3 Tarim Basin

For the Tarim Basin, only one Nd isotopic record from the Aertashi section is available from the western basin (Fig. 6c). This location is within a complex tectonic setting induced by the indentation of the Pamir, a major source of sediment after ~15 Ma, as suggested by the sudden increase in $\varepsilon_{Nd}(0)$ values approaching near-modern values in the western Tarim Basin (Fig. 6c; Blayney et al., 2016; Blayney et al., 2019). Before ~15 Ma, the $\varepsilon_{Nd}(0)$ record of the Aertashi section shows a general increase between ~41 Ma and ~25 Ma and a rapid decrease from ~25 Ma to 16 Ma. It is interesting to note that these pre-15 Ma long-term variations are quite similar to those in the eastern NTP, which suggests that the eastern and western parts of the NTP experienced in-phase provenance changes between ~41 Ma and 16 Ma. Despite this, the $\varepsilon_{Nd}(0)$ values in the western Tarim Basin fall into the range of the eastern NTP only between 30 Ma and ~16 Ma and are 0.5-1 ε_{Nd} unit higher than those in the eastern NTP at ~41-30 Ma. These two $\varepsilon_{Nd}(0)$ records diverge with a nearly constant offset before 30 Ma but converge to similar values after 30 Ma, which likely implies that the eastern and western NTP displayed slightly different source systems before 30 Ma and shared a common source and transport regime between 30 Ma and ~16 Ma.

5.2.4 The northern Tibetan Plateau as a whole

The overall picture that emerges from those different continental records is a strong similarity in the long-term Nd isotopic patterns from ~42 Ma to ~16 Ma in the frontal region of the NTP (Fig. 6c). The variation in the bulk $\varepsilon_{Nd}(0)$ values indicates a persistent increase between ~42 Ma and ~25 Ma and a significant decrease since ~25 Ma. These two periods correspond to rapid decreases in the rate of convergence between India and Eurasia (Fig. 7c; Lee and Lawver, 1995; Molnar and Stock, 2009; van Hinsbergen et al, 2011). This tectonic change has been explained by crustal thickening and uplift of the Tibetan Plateau, supported by emplacement of potassic to ultrapotassic volcanic rocks and adakites (e.g., Chung et al. 2005; Wang et al., 2010). Given the complex and contrasting Nd isotopic distributions in the modern NTP region (Fig. 5), a simple explanation for this two-stage evolution of $\varepsilon_{Nd}(0)$ values in the continental sedimentary record is a strong tectonic imprint related to the stepwise northward growth of the NTP.

Given the $\varepsilon_{Nd}(0)$ values in the Linxia and Xining Basins on the eastern NTP (Figs. 6a, 6b), the pre-existing West Qinling Mountains (Fig. 5d) could have provided initial erosional material from 50-45 Ma (Clark et al., 2010). The East Kunlun Shan and Songpan-Ganzi terrane are characterized by less negative $\varepsilon_{Nd}(0)$ values than the West Qinling Mountains (Fig. 5). Their rise in the early Cenozoic is thus expected to have delivered materials (Figs. 5b, 5c) that increased the $\varepsilon_{Nd}(0)$ values of sedimentary records in the basins. The widespread final exhumation and cooling events in the Songpan-Ganzi terrane and East Kunlun Shan regions have been dated to >40-20 Ma (Wang et al. 2014; Cao et al., 2020), with eastward extrusion of the Songpan-Ganzi Terrane starting at ~ 40 Ma (Tong et al., 2020) and rapid exhumation of the East Kunlun Shan during 40-35 Ma (Clark et al., 2010; Shi et al., 2018; Wang et al., 2017). There is a change in the $\varepsilon_{Nd}(0)$ offsets between the bulk and clay-sized material in the Xining Basin from a 1-2 ε_{Nd} unit difference before ~42 Ma to a <1 ε_{Nd} unit difference after ~42 Ma (Fig. 7d). This offset change at ~42 Ma is not associated with systematic changes in the Nd concentrations in the clay-sized samples (Table S2) or in the clay mineral contents and assemblages (Fang et al., 2019). Here, the offset change is thus assumed to be a response to this regional uplift. The $\varepsilon_{Nd}(0)$ offset is probably caused by the fact that distant sources are more significant in the clay-sized samples, while local coarse material from proximal sources is more strongly represented in the bulk samples. Therefore, the decrease in the $\varepsilon_{Nd}(0)$ offset starting at ~42 Ma and the general increase in the bulk $\varepsilon_{Nd}(0)$ values may suggest that a source far from the West Qinling Mountains with less negative $\varepsilon_{Nd}(0)$ values (e.g., the East

Kunlun Shan and Songpan-Ganzi terrane) emerged. This would imply a significant increase in the exhumation and unroofing of this potential source with less negative $\varepsilon_{Nd}(0)$ values. A relatively high level of exhumation of this remote source area is inferred because a low level of exhumation would deliver only fine-grained materials to the Xining Basin, resulting only in a visible offset between the bulk and the clay-sized material and not in significant changes in the bulk $\varepsilon_{Nd}(0)$ values. The change in the $\varepsilon_{Nd}(0)$ offset suggests a response to more regional tectonic uplift and, therefore, early uplift of the NTP region. The subsequent and more recent northern growth of the NTP exhumed material with more negative $\varepsilon_{Nd}(0)$ values (approximately -12 on average) in the Qilian Shan since the late Oligocene. The exact timing is not well defined, but the late-stage exhumation and cooling events in the Qilian-Qaidam region are all younger than 25 Ma (Wang et al., 2014). In detail, the accelerated thrust-related exhumation at 25-22 Ma in the Elashan to the east of the Qaidam Basin (Lu et al., 2012) and Laji Shan to the south of the Xining Basin (Lease et al., 2011) was accompanied by fast strike-slip motion of the Altyn Tagh fault since the early Miocene (Lu et al., 2014) and an abrupt provenance change in magnetic minerals in the Xining Basin sediments at 25-20 Ma (Xiao et al., 2012).

Although the northward migration of the exhumation of different terranes in the NTP is well documented in the eastern part of the area, only one record is available from the western Tarim Basin. However, regardless of the complex tectonic setting with variable lithologies in that area (Blayney et al., 2019; Chapman et al., 2018; Clift et al., 2017), the model of two-stage tectonic activity has stood up well and remains supported by the available evidence there. For example, backstripping analyses (Balyney et al., 2019) indicate a prominent onset of tectonic subsidence at ~41 Ma and a rapid increase in subsidence at ~25-22 Ma in the western Tarim Basin (Fig. 7f). These observations are consistent with the intensified tectonic activity in the Tarim and Tajik

Basins at ca. 41 Ma (Kaya et al., 2019), rapid exhumation and uplift of the Tian Shan-Pamir (Wang et al., 2020), foreland subsidence in the southern Tarim Basin at ~25 Ma (Jiang and Li, 2014) (Figs. 5b and 7d), and an increase in the sediment accumulation rate starting at ~ 25 Ma in central Asia (Fig. 7g, Métivier et al., 1999).

5.3 Implication for North Pacific Ocean dust records

Here, we use the only available post-40 Ma Nd isotopic record of aluminosilicate dust deposition in the NPO from core GPC3 (Fig. 5a, Pettke et al., 2002a; Zhang et al., 2016) to identify provenance changes in Asian dust. However, we need to evaluate the potential impacts of volcanogenic and authigenic materials on the aluminosilicate component of pelagic sediment (e.g., Ziegler et al., 2007) to compare similar types of material in marine and continental records. The analyses of the Nd-Pb isotopic provenance confirm that a single shale-like source (fine-grained Asian dust) has dominated the smooth Nd isotopic curve in core GPC3 since ~40 Ma, suggesting little influence of volcanogenic and authigenic materials on the $\varepsilon_{Nd}(0)$ values of the GPC3 record (Pettke et al., 2002a). In addition, the aluminosilicate component of Ocean Drilling Program (ODP) site 1215, southeast of core GPC3 in the central Pacific, began to exhibit a dominantly Asian dust source only when it moved northwestward to a paleolatitude of ~20 °N at ~20 Ma (Ziegler et al., 2007). Plate reconstruction implies that the location of core GPC3 had already reached this latitude by ~ 40 Ma (Pettke et al., 2002a). Thus, a relatively stable wind regime over the central Pacific prevailing between ~40 and ~20 Ma would have provided dominantly Asian dust since ~40 Ma at the GPC3 location. In this case, evolution of the Asian dust source has dominated the provenance evolution of core GPC3 over the past 40 Myr. Finally, the Cenozoic history of the volcanic eruptions in the circum-Pacific arcs indicates that eruption activity that formed basaltic and andesitic materials (with positive $\varepsilon_{Nd}(0)$ values) displayed a generally stable trend before ~15 Ma and a continuous increase since then (e.g., Jicha et al., 2009). This volcanic eruption evolution is inconsistent with the general Nd isotopic evolution of core GPC3. Specifically, the rise in volcanic eruption activity would be associated with a rise in the $\varepsilon_{Nd}(0)$ values in core GPC3 since 15 Ma, but the $\varepsilon_{Nd}(0)$ values in core GPC3 have decreased since 15 Ma. In summary, we argue that the eolian dust Nd isotopic records preserved in core GPC3 since ~40 Ma provide a first-order constraint on the provenance changes in fine-grained Asian dust as a whole and that the contribution of non-Asian dust sources may have been low enough since ~40 Ma to have an insignificant impact on the Nd isotopic records.

The temporal evolution of the $\varepsilon_{Nd}(0)$ values in clay-sized material in the Xining and Linxia Basins can be compared to that in the core GPC3 sediment since the extracted eolian component in core GPC3 has a median grain size of Φ 8.6-9.4 or ~3 μm and is dominated by fine-grained clay (Janecek and Rea, 1983). Dust samples can have coarse eolian grains, such as those collected in large dust storm events in sediment traps in the open ocean of the North Pacific (Betzer et al., 1988). However, the large wind-blown grains associated with such major dust storm events are extremely rare in the long-term sedimentary record in the NPO, and the dust mass influx during an entire dust storm event accounts for only < 1% of the annual average eolian sediment flux (Betzer et al., 1988). Moreover, quartz particles alone comprise ~95% of the eolian flux of > 75 μm particles by mass during dust events (Betzer et al., 1988), suggesting that large dust grains have a very small impact on the Nd budget since the Nd concentration in quartz is very low.

To produce a suitable NTP record for comparison with the NPO record, a similar type of material must be used, especially in terms of grain size. This is important for the Nd isotopic composition since the clay-sized $\varepsilon_{Nd}(0)$ values in the Linxia and Xining Basins show the same variations as the bulk sediments, but the absolute values are generally within ~1 ε_{Nd} unit higher than those of the bulk sediments since ~42 Ma (Fig. 4). Thus, the composite Nd isotope curve of NTP dust uses only values of the clay-sized fractions from the Xining and Linxia Basins. The discrete original Nd isotopes data in core GPC3 and in the Linxia and Xining Basins are linearly interpolated to produce continuous records with an interval of 0.5 Myr (Fig. 7). Since the comparison is performed over a significant period of time (40 Myr), we have to consider the effect of the in situ decay of Sm and the use of $\varepsilon_{Nd}(t)$ (the corresponding ε_{Nd} at the time of sediment deposition). Both dust Nd isotopic records mostly reflect well-mixed fine-grained materials sourced from the upper continental crust, and therefore, the Sm/Nd ratios of the dust are likely to be fairly constant. This pattern is indeed observed in the clay-sized fractions from the Xining and Linxia Basins, where the Sm/Nd value has very little variability (8.1% at 2σ level, N=59, Table S2) and is 0.182 on average, slightly higher than the Sm/Nd value of 0.173 for the upper continental crust but expected for fine grain size (e.g., McLennan et al. 1989). In addition, the minor difference (<0.5 ε_{Nd} unit) between $\varepsilon_{Nd}(t)$ and $\varepsilon_{Nd}(0)$ for post-40 Ma sediments in core GPC3 (Pettke et al. 2002a) suggests that Sm in situ decay may exert a very limited impact relative to the variability as large as ~ 3 ε_{Nd} units in both records (Fig. 7a).

The composite dust $\varepsilon_{Nd}(0)$ values yield a gradually increasing trend from ~42 Ma to ~30 Ma, a stable composition between ~30 and ~25 Ma, and a long-term decreasing trend since ~25 Ma (Fig. 7a). The core GPC3 $\varepsilon_{Nd}(0)$ values generally exhibit a trend similar to that of the NTP data between ~40 and ~25 Ma, with an absolute value ~ 0.5 ε_{Nd} units higher during ~30-38 Ma (Fig. 7a). After ~25 Ma, there are significant offsets as large as ~2 ε_{Nd} units between the NTP and the NPO. Considering the uncertainties in the $\varepsilon_{Nd}(0)$ values, the offsets are still significant (Fig. 7a). The main tectonic events around the CAOB region that were responsible for the provenance regime (Fig. 1) occurred before the Cenozoic (e.g., Zheng et al., 2013, and section 5.1). The $\varepsilon_{Nd}(0)$ contrast, as seen in modern settings between the NTP and CAOB, could have existed over the past 40 Myr. Moreover, the Cenozoic tectonic changes in the NTP, such as the early exhumation of the East Kunlun Shan and Songpan-Ganzi Terrane, are taken into account in the composite NTP dust record (Fig. 7). Therefore, the increase in the offset between the NTP and the NPO at ~25 Ma clearly reflects an increase in the contribution of the CAOB to Asian dust.

A simplified quantitative mass balance calculation can show the relative contributions of the NTP and the CAOB to the NPO. The ^{143}Nd/^{144}Nd value of clay-sized dust from the Asian interior that can be transported to the NPO can be described from a mixing perspective:

$$\frac{^{143}\mathrm{Nd}}{^{144}\mathrm{Nd}}\mathrm{NPO} = \frac{f \times [\mathrm{Nd}]_{\mathrm{NTP}} \times \frac{^{143}\mathrm{Nd}}{^{144}\mathrm{Nd}}\mathrm{NTP} + (1-f) \times [\mathrm{Nd}]_{\mathrm{CAOB}} \times \frac{^{143}\mathrm{Nd}}{^{144}\mathrm{Nd}}\mathrm{CAOB}}{f \times [\mathrm{Nd}]_{\mathrm{NTP}} + (1-f) \times [\mathrm{Nd}]_{\mathrm{CAOB}}} \tag{1}$$

where *f* denotes the NTP contribution to the NPO dust and [Nd] is the Nd concentration in the eolian clay-sized material. Here, we use the measured Nd concentration and ^{143}Nd/^{144}Nd value in our clay-sized samples from the Linxia and Xining Basins to constrain the evolving NTP endmember since 40 Ma. The CAOB endmember is assumed to be constant due to the nonexistence of a long-term temporal record. The CAOB endmember can be constrained by the average ^{143}Nd/^{144}Nd value (0.512358±0.000264, corresponding to $\varepsilon_{\mathrm{Nd}}(0)$=-5.5, 2σ, n=29) and Nd concentration (34.9±21.8 μg/g, 2σ, n=11) of the <2 μm fraction of Gobi and desert sediments in northern China and southern Mongolia (Table S3; Zhao et al., 2014, 2015). For consistency with the $\varepsilon_{\mathrm{Nd}}(0)$ values (Fig. 7), the discrete original Nd isotopic and concentration data in core GPC3 and in the Linxia and Xining Basins are linearly interpolated with an interval of 0.5 Myr. The denominator on the right-hand side of equation (1) uses the mixed Nd concentration from the NTP and the CAOB rather than the Nd concentrations of the NPO samples (e.g., core GPC3) because we assume that the dust Nd isotope is more stable than the Nd concentration during the long-distance transport to the NPO. That is, the Nd concentration measured in the NPO samples probably depends not only on the dust mixing proportions from two distinct dust source areas but also on other processes, e.g., the sorting process during transport, while the dust Nd isotopic compositions are less affected during the long-distance transport. The Nd isotope stability could be demonstrated by the nearly constant Nd isotopes ($\varepsilon_{Nd}(0)$ ranging from -10.1 to -10.9) for modern eolian silicate dust collected at the varying sites in the broader NPO central province (Pettke et al., 2002b). With such assumptions, the estimated NTP contribution to the NPO ranges from 58% to 100%, showing the dominant role of NTP contributions to NPO dust over the last 40 Myr. The CAOB contribution reaches its maximum (~40%) between ~25 and ~13 Ma, with a significant, albeit smaller (~20%), contribution between ~35 and ~33 Ma (Fig. 7b). The changes in the Nd concentration in <2 μm CAOB sediments (1σ change of mean from 24 to 46 μg/g) exhibit a limited deviation (<8% of NTP contribution) compared with the curve reconstructed from the mean Nd concentration (Fig. 6b), which does not change the general pattern of the NTP contribution over the last 40 Myr. Such a pattern of the NTP contribution reconstructed from the mean $\varepsilon_{Nd}(0)$ value (-5.5) and mean Nd concentration (34.9 μg/g) remains unchanged when using different constant CAOB endmembers with $\varepsilon_{Nd}(0)$=-1, -3, and -7 (Fig. 7b). The range from -1 to -7 covers most $\varepsilon_{Nd}(0)$ values for the <2 μm fraction of surface sediments in the CAOB (Zhao et al., 2014, Table S3). Our above observations are thus valid if a provenance change in the CAOB had occurred within an $\varepsilon_{Nd}(0)$ range of -1 to -7 during the past 40 Myr. It should be noted here that because the NTP and core GPC3 Nd isotopic records are discrete and spiky, uncertainties in the calculation for a given data point will be large based on the linear interpolation approach. Therefore, the estimated general pattern of the NTP contribution and an average value for a given period are more convincing than any single data point.

However, the small CAOB peak at approximately 33-36 Ma signifies the occurrence of a more radiogenic source for the NPO than for the NTP. This could be the CAOB, but it could also correspond to dust from a further western source since the western Tarim Basin is likely to produce dust with $\varepsilon_{Nd}(0)$ values higher than ~1 ε_{Nd} units in the Xining Basin (Fig. 6c). The lack of clay-sized sedimentary records in the Tarim Basin prevents its inclusion in the composite history of NTP dust Nd isotopic variations. Here, we apply two sensitivity tests to check whether the Tarim Basin with higher ε_{Nd} values before ~30 Ma could have acted as an independent source endmember accounting for this small apparent CAOB peak. The Tarim dust Nd isotopic endmember is obtained by assuming that the ε_{Nd} values of <2 μm Tarim sediment are ~0.5 ε_{Nd} unit higher than those of bulk sediments (bulk ε_{Nd} values are from Blayney et al., 2019, Fig. 6c). The assumed ~0.5 ε_{Nd} unit difference is similar to the mean ε_{Nd} offset between the <2 μm and bulk sediments after 42 Ma in the Xining Basin (as shown in Fig. 7d). To simplify the tests, the change in Tarim dust Nd concentration before 25 Ma is assigned to be identical to that of the <2 μm fraction of the Xining sediments. The results show that 1) when the NTP endmember is fully represented by Tarim Basin composition (100% Tarim, bold violet line in Fig. 6b), the NTP contribution is mostly greater than 100% before ~ 30 Ma with a negligible CAOB contribution and is characterized by a minimum of approximately 100% at 33-36 Ma; 2) when the NTP endmember is composed of 50% Tarim Basin and 50% Xining compositions (bold blue line in Fig. 6b), there is a significantly reduced CAOB peak of approximately 10-15% at 33-36 Ma. The above tests thus suggest that the inclusion of a varying proportion of Tarim dust with high ε_{Nd} values in the whole NTP endmember before 30 Ma could explain the apparent CAOB peak. This CAOB peak reaches its maximum at approximately 33-35 Ma, which is consistent with the global cooling at ~34 Ma known as the Eocene–Oligocene climate transition (Zachos et al., 2001). This global cooling, with the expansion of ice sheets in the Antarctic at ~ 34 Ma, would have resulted in a decline in the westerly-carried moisture transported to the Tarim Basin, a drop in sea level and a further retreat of the Paratethys Sea, thereby lengthening the distance between the Tarim Basin and the moisture source (e.g., Kaya et al., 2019; Ye et al. 2020). As a consequence, regional drying may have promoted dust emissions and transport from the Tarim Basin to the NPO region.

The later CAOB peak after 25 Ma is more likely to be related to the CAOB contribution because the sharp increase from <10% at ~30-25 Ma to ~30-40% after ~25 Ma coincided temporally with the onset of eolian deposition in Central Asia (Sun et al., 2010; Zheng et al., 2015) and the CLP (Guo et al., 2002; Qiang et al., 2011). In principle, there are two conceptual models that can account for the increase in the CAOB contribution to Asian dust in the late Oligocene. One corresponds to major climatic reorganization and is based on a poleward shift of the westerlies capable of transporting more CAOB-derived dust to the NPO. This scenario seems unlikely. The wandering of the westerlies is well described at the glacial-interglacial time scale (e.g., Pullen et al., 2011; Toggweiler et al., 2006; Fig. 1a) and at longer time scales (mid-Pliocene warm period from 3.3-3.0 Ma, Li et al., 2015). Therefore, if the late Pliocene and Quaternary climatic variations are representative of the effects of long-term climatic cooling since the late Oligocene, an equatorward shift in the westerlies would be associated with cooling. Such southward migration of the westerlies should deliver more materials from the NTP but not produce a relative increase in the CAOB contribution to the NPO. The alternative model suggests that tectonic exhumation is the primary factor that changes the relative proportions of sources of Asian dust delivered to the NPO. In this case, the increase in the CAOB contribution was mainly caused by exhumation of the CAOB under a more favorable climatic regime for dust production since the late Oligocene. First, the Eocene retreat of the Para-Tethys Sea not only promoted aridification of the Asian interior

(Kaya et al., 2019; Ramstein et al., 1997) but also exposed large areas of continental surfaces to wind erosion. Second, as a far-field effect of the India-Asia collision, the onset of deformation and mountain uplift in central Asia occurred in the Oligocene to the early Miocene (e.g., Charreau et al., 2009; Caves et al., 2014; Ji et al., 2008; Li et al., 2020; Sobel et al., 2006; Wang et al., 2020; Yuan et al., 2006) and played a key role in the intensification of regional aridification and dust emissions (Caves et al., 2014; Sun and Liu, 2018). Third, the rapid uplift of the Tibetan Plateau in the late Oligocene (~26 Ma, Lu et al., 2018) could have induced more intense aridification of the Asian interior, as suggested by climatic modeling (e.g., Tada et al., 2016). Taken together, all of the above factors facilitated the formation of a topographic and climatic regime in the Asian interior that was highly favorable to the emission and transport of eolian dust (Fig. 8a). The significant contribution of CAOB material to Asian dust systems since the late Oligocene has highlighted the close linkage between large-scale dust emissions and tectono-climatic evolution. This scenario contrasts with the regime prior to the late Oligocene, which was characterized by low relief in the CAOB region (Fig. 8b; Ji et al., 2008; Sobel et al., 2006; Yuan et al., 2016).

In addition, the CAOB contribution has decreased for the last ~13 Myr (Fig. 7b), while the absolute dust accumulation in the NPO has risen sharply (Janecek and Rea, 1983; Zhang et al., 2016; Fig. 7). The decrease in the CAOB contribution since ~13 Ma is only relative to the NTP contribution. If such a decrease is also associated with a doubling of the overall Asian dust production (the mass accumulation rate in the NPO suggests that a rise by a factor of 2 is quite conservative, Figs. 7h and 7i), the CAOB is likely to have produced at least the same amount of dust, while the dust production in the NTP would have more than doubled. There are many lines of evidence suggesting the acceleration of uplift and outward growth of the Qilian Shan in the eastern NTP (e.g., Chen et al., 2019; Li et al., 2019; Zhuang et al., 2019) and of the western NTP (e.g., Cao et al., 2013; Jiang and Li, 2014; Sobel et al., 2013). There are also many lines of evidence for enhanced tectonic uplift in the CAOB region (e.g., Caves et al., 2014; Charreau et al. 2009; Ji et al., 2008; Xiang et al. 2019). Moreover, global cooling since 14 Ma (Zachos et al., 2001) has reduced the amount of vapor held in the atmosphere and expanded the arid belt in the Asian interior. This close interplay between middle to late Miocene tectonic exhumation and global cooling promoted dust emissions in the Asian interior, accounting for the persistent increases in the eolian mass accumulation rate at ODP site 1208 and core GPC3 in the NPO (Fig. 7i; Janecek and Rea, 1983; Zhang et al., 2016). In addition, the relative decrease in the CAOB contribution since ~13 Ma might also have been partly caused by an equatorward shift in the westerlies associated with global cooling and the build-up of the Siberian High climatic system (e.g., Li et al., 2015; Pullen et al., 2011; Toggweiler et al., 2006). Finally, the rise and outward growth of the Qilian Shan not only promoted dust emissions and deposition on the CLP (Sun and Liu, 2018) but also intensified the transport of dust from the Erdos Basin with very negative $\varepsilon_{Nd}(0)$ values (Fig. 5b) to the NPO. The latter process could have been forced by enhanced monsoon-driven erosion (e.g., Nie et al., 2018) and may also have contributed to the decrease in $\varepsilon_{Nd}(0)$ values in core GPC3.

6 CONCLUSIONS

Our study reveals clear and consistent provenance changes in the NTP based on Nd isotopic records from both bulk and clay-sized sediments. The Cenozoic provenance changes in the NTP are characterized by a gradual increase in $\varepsilon_{Nd}(0)$ values between ~42 Ma and ~25 Ma and a general decrease since ~25 Ma. This temporal evolution can be explained by the two-stage northward growth of the Tibetan Plateau. The comparison of the Nd isotopic variation in dust from the NTP with that in sediment in core GPC3 from the NPO suggests that a detectable, yet not quantified, contribution from the western Tarim Basin occurred between ~38 and ~30 Ma and that the contribution of the CAOB to Asian dust has been present since ~25 Ma. The sharp late Oligocene increase in the CAOB contribution to Asian dust is consistent with the establishment of eolian systems in central Asia and east Asia, suggesting that a modern tectonic climate regime favoring the formation and transport of Asian dust is likely to have initiated in the late Oligocene.

ACKNOWLEDGMENTS

This study was co-supported by the Strategic Priority Research Program of the Chinese Academy of Sciences (XDA20070201), the Second Tibetan Plateau Scientific Expedition and Research (2019QZKK0707), the National Natural Science Foundation of China (41771236, 41620104002), and the Basic Science Center for Tibetan Plateau Earth System (41988101-01). Y. Yang was supported by the Youth Innovation Promotion Association (2018095) of the Chinese Academy of Sciences. Wenbo Rao is thanked for providing Tarim data, and Lin Ma is thanked for useful discussion. The authors thank Associate Editor Prof. Franco Marcantonio and three anonymous reviewers for their thoughtful and constructive comments. Special thanks go to Reviewer #1 and the AJE editors for their great efforts in proofreading and polishing the language.

SUPPLEMENTARY MATERIAL

The Electronic Annex, including Tables S1-S3 is specific the Research Data associated with this manuscript.

REFERENCES

Blayney T., Najman Y., Dupont-Nivet G., Carter A., Millar I., Garzanti E., Sobel E. R., Rittner M., Ando S., Guo Z., Vezzoli G. (2016) Indentation of the Pamirs with respect to the northern margin of Tibet: Constraints from the Tarim basin sedimentary record. *Tectonics* **35**(10), 2345-2369.

Blayney T., Dupont-Nivet G., Najman Y., Proust J. N., Meijer N., Roperch P., Sobel E. R., Millar I. and Guo, Z. (2019) Tectonic evolution of the Pamir recorded in the western Tarim Basin

(China): sedimentologic and magnetostratigraphic analyses of the Aertashi section. *Tectonics* **38**(2), 492-515.

Betzer P. R., Carder K. L., Duce R. A., Merrill J. T., Tindale N. W., Uematsu M., Costello D. K., Young R. W., Feely R. A., Breland J. A. and Bernstein R. E. (1988) Long-range transport of giant mineral aerosol particles. *Nature* **336**(6199), 568-571.

Cao K., Wang G., van der Beek P., Bernet M. and Zhang K. (2013) Cenozoic thermo-tectonic evolution of the northeastern Pamir revealed by zircon and apatite fission-track thermochronology. *Tectonophysics* **589**, 17-32.

Cao K., Leloup P. H., Wang G., Liu W., Mahéo G., Shen T., Xu Y., Sorrel P. and Zhang K. (2020) Thrusting, exhumation, and basin fill on the western margin of the South China block during the India-Asia collision. *Geol. Soc. Am. Bull.* https://doi.org/10.1130/B35349.1.

Caves J. K., Sjostrom D. J., Mix H. T., Winnick M. J. and Chamberlain C. P. (2014) Aridification of Central Asia and uplift of the Altai and Hangay Mountains, Mongolia: Stable isotope evidence. *Am. J. Sci.* **314**(8), 1171-1201.

Chapman J. B., Scoggin S. H., Kapp P., Carrapa B., Ducea M. N., Worthington J., Oimahmadov I. and Gadoev M. (2018) Mesozoic to Cenozoic magmatic history of the Pamir. *Earth Planet. Sci. Lett.* **482**, 181-192.

Chang Q., Mishima T., Yabuki S., Takahashi Y. and Shimizu H. (2000) Sr and Nd isotope ratios and REE abundances of moraines in the mountain areas surrounding the Taklimakan Desert, NW China. *Geochem. J.* **34**(6), 407-427.

Charreau J., Chen Y., Gilder S., Barrier L., Dominguez S., Augier R., Sen A., Avouac J-P., Gallaud A., Graveleau F., Wang Q. C., Konca A. O., Sladen A., Meltzner A. J., Sieh K., Fang P., Li Z. H., Galetzka J., Genrich J., Chlieh M., Natawidjaja D. H., Bock Y., Fielding E. J., Ji C., Helmberger D., Leprince S., Muse P. and Taylor M. H. (2009) Neogene uplift pulses of the Tianshan mountains observed in the magnetic record of the Jingou River section (Northwest China). *Tectonics* **28**(2), 224-243.

Che X., Li G. (2013) Binary sources of loess on the Chinese Loess Plateau revealed by U–Pb ages of zircon. *Quat. Res.*, **80**(3), 545-551.

Chen J., Li G. J., Yang J. D., Rao W. B., Lu H. Y., Balsam W., Sun Y. B. and Ji J. F. (2007) Nd and Sr isotopic characteristics of Chinese deserts: implications for the provenances of Asian dust. *Geochim. Cosmochim. Acta* **71**(15), 3904-3914.

Chen J. and Li G. (2011) Geochemical studies on the source region of Asian dust. *Sci. China Earth Sci.* **54**(9), 1279-1301.

Chen Z. and Li G. (2013) Evolving sources of eolian detritus on the Chinese Loess Plateau since early Miocene: Tectonic and climatic controls. *Earth Planet. Sci. Lett.* **371**, 220-225.

Chung S. L., Chu M. F., Zhang Y. Q., Xie Y. W., Lo C. H., Lee T. Y., Lan C. Y., Li X. H., Zhang Q. and Wang Y. Z. (2005) Tibetan tectonic evolution inferred from spatial and temporal variations in post-collisional magmatism. *Earth-Sci. Rev.* **68**(3-4),173-196.

Clark M. K., Farley K. A., Zheng D., Wang Z. and Duvall, A. R. (2010) Early Cenozoic faulting of the northern Tibetan Plateau margin from apatite (U-Th)/He ages. *Earth Planet. Sci. Lett.* **296**(1-2), 78-88.

Clift P. D., Zheng H., Carter A., Böning P., Jonell T. N., Schorr H., Shan X., Pahnke K., Wei X. and Rittenour, T. M. (2017) Controls on erosion in the western Tarim Basin: Implications for the uplift of northwest Tibet and the Pamir. *Geosphere* **13**(5), 1747-1765.

Dai S., Fang X., Dupont-Nivet G., Song C., Gao J., Krijgsman Langereis C. and Zhang W. (2006) Magnetostratigraphy of Cenozoic sediments from the Xining Basin: tectonic implications for the northeastern Tibetan Plateau. *J. Geophys. Res.* **111**(B11), B11102.

Ding L., Xu Q., Yue Y., Wang H., Cai F. and Li S. (2014). The Andean-type Gangdese Mountains: Paleoelevation record from the Paleocene–Eocene Linzhou Basin. *Earth Planet. Sci. Lett.* **392**, 250-264.

Du S., Wu Y. and Tan L. (2018) Geochemical evidence for the provenance of aeolian deposits in the Qaidam Basin, Tibetan Plateau. *Aeolian Res.* **32**, 60-70.

Fan M., Song C., Dettman D. L., Fang X. and Xu X. (2006) Intensification of the Asian winter monsoon after 7.4 Ma: grain-size evidence from the Linxia Basin, north-eastern Tibetan Plateau, 13.1 Ma to 4.3 Ma. *Earth Planet. Sci. Lett.* **248**, 186-197.

Fang X., Garzione C. N., Van der Voo R., Li J. and Fan M. (2003) Flexural subsidence by 29 Ma on the NE edge of Tibet from the magnetostratigraphy of Linxia basin, China. *Earth Planet. Sci. Lett.* **210**, 545-560.

Fang X., Wang J., Zhang W., Zan J., Song C., Yan M., Appel E., Zhang T., Wu F., Yang Y. and Lu Y. (2016) Tectonosedimentary evolution model of an intracontinental flexural (foreland) basin for paleoclimatic research. *Glob. Planet. Change* **145**, 78-97.

Garzione C. N., Ikari M. J. and Basu, A. R. (2005) Source of Oligocene to Pliocene sedimentary rocks in the Linxia basin in northeastern Tibet from Nd isotopes: Implications for tectonic forcing of climate. *Geol. Soc. Am. Bull.* **117**(9), 1156-1166.

Guo Z. T., Ruddiman W. F., Hao Q. Z., Wu H. B., Qiao Y. S., Zhu R. X., Peng S. Z., Wei J. J., Yuan B. Y. and Liu T. S. (2002) Onset of Asian desertification by 22 Myr ago inferred from loess deposits in China. *Nature* **416**(6877), 159-163.

He Z., Guo Z., Yang F., Sayem A. S. M., Wu H., Zhang C., Hao Q., Xiao G., Han L., Fu Y., Wu Z. and Hu, B. (2019) Provenance of Cenozoic sediments in the Xining Basin revealed by Nd and Pb isotopic evidence: Implications for tectonic uplift of the NE Tibetan Plateau. *Geochem. Geophys. Geosyst.* **20**(10), 4531-4544.

Jacobsen S. B., Wasserburg G. J. (1980) Sm-Nd isotopic evolution of chondrites. *Earth Planet. Sci. Lett.* **50**, 139-155.

Janecek T. R. and Rea D. K. (1983) Eolian deposition in the northeast Pacific Ocean: Cenozoic history of atmospheric circulation. *Geol. Soc. Am. Bull.* **94**(6), 730-738.

Ji J., Luo P., White P., Jiang H., Gao L. and Ding, Z. (2008) Episodic uplift of the Tianshan Mountains since the late Oligocene constrained by magnetostratigraphy of the Jingou River section, in the southern margin of the Junggar Basin, China. *J. Geophys. Res.-Solid Earth* **113**(B5), B05102.

Jiang X. D. and Li, Z. X. (2014) Seismic reflection data support episodic and simultaneous growth of the Tibetan Plateau since 25 Myr. *Nat. Commun.* **5**, 5453.

Jicha B. R., Scholl D. W. and Rea, D. K. (2009) Circum-Pacific arc flare-ups and global cooling near the Eocene-Oligocene boundary. *Geology* **37**(4), 303-306.

Kaya M. Y., Dupont-Nivet G., Proust J. N., Roperch P., Bougeois L., Meijer N., Frieling J., Fioroni C., Altiner A. O., Vardar E., Barbolini N., Stoica M., Aminov J., Mamtimin M. and Guo Z. J. (2019) Paleogene evolution and demise of the proto-Paratethys Sea in Central Asia (Tarim and Tajik basins): role of intensified tectonic activity at ca. 41 Ma. *Basin Res.* **31**(3), 461-486.

Laborde A., Barrier L., Simoes M., Li H., Coudroy T., Van der Woerd J. and Tapponnier P. (2019) Cenozoic deformation of the Tarim Basin and surrounding ranges (Xinjiang, China): A regional overview. *Earth-Sci. Rev.* **197**, 102891.

Lamb, M. A. and Badarch, G. (1997) Paleozoic sedimentary basins and volcanic-arc systems of southern Mongolia: New stratigraphic and sedimentologic constraints. *Int. Geol. Rev.*, **39**(6), 542-576.

Law R. and Allen, M. B. (2020) Diachronous Tibetan Plateau landscape evolution derived from lava field geomorphology. *Geology* **48**(3): 263-267.

Lease R. O., Burbank D. W., Clark M. K., Farley K. A., Zheng D. W. and Zhang, H. P. (2011) Middle Miocene reorganization of deformation along the northeastern Tibetan Plateau. *Geology* **39**(4), 359-362.

Lee, T. Y. and Lawver L. A. (1995) Cenozoic plate reconstruction of Southeast Asia. *Tectonophysics*, **251**(1-4), 85-138.

Li B., Chen X., Zuza A. V., Hu D., Ding W., Huang P. and Xu, S. (2019) Cenozoic cooling history of the North Qilian Shan, northern Tibetan Plateau, and the initiation of the Haiyuan fault: Constraints from apatite-and zircon-fission track thermochronology. *Tectonophysics* **751**, 109-124.

Li C., Zheng D., Sun J., Yu J., Ma Y., Zhang H., Wang Y., Pang J., Li Y. and Hao Y. (2020) Reconstruction on regional paleo-drainage evolution in the northern Junggar Basin, China during the last ~27 Myr from provenance analyses and its implications for uplift of the Altai Mountains. *Palaeogeogr. Palaeoclimatol. Palaeoecol.* **537**, 109373.

Li G., Ji J., Chen, J. and Kemp D. B. (2009) Evolution of the Cenozoic carbon cycle: the roles of tectonics and CO_2 fertilization. *Glob. Biogeochem. Cycle* **23**(1), GB1009.

Li G., Pettke T. and Chen J. (2011) Increasing Nd isotopic ratio of Asian dust indicates progressive uplift of the north Tibetan Plateau since the middle Miocene. *Geology* **39**,199-202.

Li X., Jiang D., Zhang Z., Zhang R., Tian Z. and Yan Q. (2015) Mid-Pliocene westerlies from PlioMIP simulations. *Adv. Atmos. Sci.* **32**(7), 909-923.

Licht A., Pullen A., Kapp P. Abell J. and Giesler N. (2016) Eolian cannibalism: Reworked loess and fluvial sediment as the main sources of the Chinese Loess Plateau. *Geol. Soc. Am. Bull.* **128**(5-6), 944-956.

Liu C. Q., Masuda A., Okada A., Yabuki S. and Fan, Z. L. (1994). Isotope geochemistry of Quaternary deposits from the arid lands in northern China. *Earth Planet. Sci. Lett.*, **127**(1-4), 25-38.

Liu S., Li J., Stockli D. F., Song C., Guo B., Stockli L. D., Ma Z., Li X. and Peng T. (2019) Reappraisal of Miocene eolian deposition in Tianshui Basin, China, based on an investigation of stratigraphy and provenance. *Geol. Soc. Am. Bull.* **131**(7-8), 1312-1332.

Lu H., Wang E., Shi X. and Meng, K. (2012) Cenozoic tectonic evolution of the Elashan range and its surroundings, northern Tibetan Plateau as constrained by paleomagnetism and apatite fission track analyses. *Tectonophysics* **580**, 150-161.

Lu H., Wang E. and Meng K. (2014) Paleomagnetism and anisotropy of magnetic susceptibility of the Tertiary Janggalsay section (southeast Tarim basin): Implications for Miocene tectonic evolution of the Altyn Tagh Range. *Tectonophysics* **618**, 67-78.

Lu H., Tian X., Yun K. and Li H. (2018) Convective removal of the Tibetan Plateau mantle lithosphere by ~26 Ma. *Tectonophysics* **731**, 17-34.

McLennan S. M., McCulloch M. T. Taylor S. R. and Maynard J. B. (1989) Effects of sedimentary sorting on neodymium isotopes in deep-sea turbidites. *Nature* **337**(6207), 547-549.

McLennan S. M., Hemming S., McDaniel D. K. and Hanson G. N. (1993) Geochemical approaches to sedimentation, provenance, and tectonics. In *Processes Controlling the Composition of Clastic Sediments* (eds. M. G. Johnson and A. Basu,). *Spec. Pap., Geol. Soc. Am.*, **284**, 21-21.

Métivier F. and Gaudemer Y. (1999) Stability of output fluxes of large rivers in South and East Asia during the last 2 million years: implications on floodplain processes. *Basin Res.* **11**(4), 293-303.

Molnar P. and Stock J. M. (2009) Slowing of India's convergence with Eurasia since 20 Ma and its implications for Tibetan mantle dynamics. *Tectonics* **28**(3), TC3001.

Nakano T., Yokoo Y., Nishikawa M. and Koyanagi H. (2004) Regional Sr-Nd isotopic ratios of soil minerals in northern China as Asian dust fingerprints. *Atmos. Environ.* **38**(19), 3061-3067.

Nie J., Pullen A., Garzione C. N., Peng W., and Wang Z. (2018) Pre-Quaternary decoupling between Asian aridification and high dust accumulation rates. *Sci. Adv.* **4**(2), eaao6977.

Pan Y. (1990) Tectonic features and evolution of the western Kunlun Mountain region. *Sci. Geol. Sin.* **3**, 224-32 (in Chinese with English abstract)

Pan Y. (1996) Regional geologic evolution and conclusion. In *Geologic Evolution of the Karakorum and Kunlun Mountains*, (eds. Y. Pan). Seismological Press, Beijing. pp. 263-288.

Pettke T., Halliday A. N. and Rea D. K. (2002a) Cenozoic evolution of Asian climate and Sources of Pacific seawater Pb and Nd derived from eolian dust of sediment core LL44-GPC3. *Paleoceanography* **17**(3), 3-1-3-13.

Pettke T., Lee D. C., Halliday A. N., and Rea D. K. (2002b). Radiogenic Hf isotopic compositions of continental eolian dust from Asia, its variability and its implications for seawater Hf. *Earth Planet. Sci. Lett.* **202**(2), 453-464.

Pin C. and Zalduegui J. F. S. (1997) Sequential separation of light rare-earth elements, thorium and uranium by miniaturized extraction chromatography: Application to isotopic analyses of silicate rocks. *Anal. Chim. Acta* **339**, 79-89.

Pullen A., Kapp P., McCallister A.T., Chang H., Gehrels G.E., Garzione C. N., Heermance R.V. and Ding L. (2011) Qaidam Basin and northern Tibetan Plateau as dust sources for the Chinese Loess Plateau and paleoclimatic implications. *Geology* **39**, 1031-1034.

Qiang X., An Z., Song Y., Chang H., Sun Y., Liu W., Ao H., Dong J., Fu C., Wu F., Lu F., Cai Y., Zhou W., Cao J., Xu X. and Ai L. (2011) New eolian red clay sequence on the western Chinese Loess Plateau linked to onset of Asian desertification about 25 Ma ago. *Sci. China-Earth Sci.* **54**(1), 136-144.

Ramstein G., Fluteau F., Besse J. and Joussaume S. (1997) Effect of orogeny, plate motion and land-sea distribution on Eurasian climate change over the past 30 million years. *Nature* **386**(6627), 788-795.

Rao W., Tan H., Chen J., Ji J., Chen Y., Pan Y. and Zhang W. (2015) Nd-Sr isotope geochemistry of fine-grained sands in the basin-type deserts, west China: implications for the source mechanism and atmospheric transport. *Geomorphology* **246**, 458-471.

Rea D. K., Snoeckx H. and Joseph L. H. (1998) Late Cenozoic eolian deposition in the North Pacific: Asian drying, Tibetan uplift, and cooling of the Northern Hemisphere. *Paleoceanography* **13**(3), 215-224.

Ruan X., Yang Y., Galy A., Fang X., Jin Z., Zhang F., Yang R., Deng L., Meng Q., Ye C. and Zhang W. (2019) Evidence for early (≥ 12.7 Ma) eolian dust impact on river chemistry in the northeastern Tibetan Plateau. *Earth Planet. Sci. Lett.*, **515**, 79-89.

Shi W., Wang F., Wu L., Yang L., Zhang W. and Wang Y. (2018) A prolonged Cenozoic erosional period in East Kunlun (Western China): Constraints of detrital apatite (U-Th)/He ages on the onset of mountain building along the northern margin of the Tibetan Plateau. *J. Asian Earth Sci.* **151**, 54-61.

Sobel E. R., Chen J. and Heermance R. V. (2006) Late Oligocene-Early Miocene initiation of shortening in the Southwestern Chinese Tian Shan: Implications for Neogene shortening rate variations. *Earth Planet. Sci. Lett.* **247**, 70-81.

Sobel E. R., Chen J., Schoenbohm L. M., Thiede R., Stockli D. F., Sudo M. and Strecker M. R. (2013) Oceanic-style subduction controls late Cenozoic deformation of the Northern Pamir orogen. *Earth Planet. Sci. Lett.* **363**, 204-218.

Stuut J. B., Zabel M., Ratmeyer V., Helmke P., Schefuß E., Lavik G. and Schneider R. (2005) Provenance of present‐day eolian dust collected off NW Africa. *J Geophys. Res-Atmos.* **110**, D04202.

Sun J., Ye J., Wu W., Ni X., Bi S., Zhang Z., Liu W. and Meng, J. (2010) Late Oligocene-Miocene mid-latitude aridification and wind patterns in the Asian interior. *Geology* **38**(6), 515-518.

Sun H. and Liu X. (2018) Impacts of the uplift of four mountain ranges on the arid climate and dust cycle of inland Asia. *Palaeogeogr. Palaeoclimatol. Palaeoecol.* **505**, 167-179.

Tada R., Zheng H. and Clift P. D. (2016) Evolution and variability of the Asian monsoon and its potential linkage with uplift of the Himalaya and Tibetan Plateau. *Prog. Earth Planet. Sci.* **3**(1), 4.

Tanaka T., Ogashi S., Kamioka H., Amakawa H., Kagami H., Hamamoto T., Yuhara M., Orihashi Y., Yoneda S., Shimizu H., Kunimaru T., Takahashi K., Yanagi T., Nakano T., Fujimaki H., Shinjo R., Asahara Y., Tanimizu M. and Dragusanu C. (2000) JNdi-1: a neodymium isotopic reference in consistency with LaJolla neodymium. *Chem. Geol.* **168**, 279-281.

Tapponnier P., Xu Z., Roger F., Meyer B., Arnaud N., Wittlinger G. and Yang J. (2001). Oblique stepwise rise and growth of the Tibet Plateau. *Science* **294**(5547), 1671-1677.

Toggweiler J. R., Russell J. L. and Carson S. R. (2006) Midlatitude westerlies, atmospheric CO_2, and climate change during the ice ages. *Paleoceanography* **21**(2), PA2005.

Tong Y., Wu Z., Yujun S., Yang Z., Pei J., Yang X., Li J. and Wang C. (2020) The interaction of the eastward extrusion of the Songpan-Ganzi Terrane and the crustal rotational movement of the Sichuan Basin since the Late Paleogene: Evidence from Cretaceous and Paleogene paleomagnetic datasets of the Sichuan Basin. *Tectonics* **39**(2), e2019TC005784.

van Hinsbergen D. J. J., Steinberger B., Doubrovine P. V. and Gassmoller R. (2011) Acceleration and deceleration of India-Asia convergence since the Cretaceous: roles of mantle plumes and continental collision. *J. Geophys. Res.-Solid Earth* **116**, B06101.

Wang C., Dai J., Zhao X., Li Y., Graham S. A., He D., Ran B. and Meng J. (2014) Outward-growth of the Tibetan Plateau during the Cenozoic: A review. *Tectonophysics* **621**, 1-43.

Wang F., Shi W., Zhang W., Wu L., Yang L., Wang Y. and Zhu R. (2017) Differential growth of the northern Tibetan margin: evidence for oblique stepwise rise of the Tibetan Plateau. *Sci. Rep.* **7**(1), 1-9.

Wang Q., Wyman D. A., Li Z. X., Sun W., Chung S. L., Vasconcelos P. M., Zhang Q., Dong H., Yu Y., Pearson N., Qiu H., Zhu T., Feng X. (2010) Eocene north–south trending dikes in central Tibet: new constraints on the timing of east–west extension with implications for early plateau uplift?. *Earth Planet. Sci. Lett.* **298**(1-2), 205-216.

Wang X., Carrapa B., Chapman J. B., Henriquez S., Wang M., DeCelles P. G., Li Z., Wang F., Oimuhammadzoda I., Gadoev M. and Chen, F. (2019). Parathethys last gasp in central Asia and late Oligocene accelerated uplift of the Pamirs. *Geophys. Res. Lett.* **46**(21), 11773-11781.

Wang Y., Zhang J., Qi W. and Guo S. (2015) Exhumation history of the Xining Basin since the Mesozoic and its tectonic significance. *Acta Geol. Sin. (English Edition)* **89**, 145-162.

Wasserburg G. J., Jacobsen S. B., DePaolo D. J., McCulloch M. T. and Wen T. (1981) Precise determination of Sm/Nd ratios, Sm and Nd isotopic abundances in standard solutions. *Geochim. Cosmochim. Acta* **45**, 2311-2323.

Wilson D. J., Piotrowski A. M., Galy A. and McCave I. N. (2012) A boundary exchange influence on deglacial neodymium isotope records from the deep western Indian Ocean. *Earth Planet. Sci. Lett.* **341-344**, 35-47.

Wilson D. J., Piotrowski A. M., Galy A., Clegg J. A. (2013) Reactivity of neodymium carriers in deep sea sediments: implications for boundary exchange and paleoceanography. *Geochim. Cosmochim. Acta* **109**, 197-221.

Windley B. F., Alexeiev D., Xiao W., Kröner A. and Badarch, G. (2007) Tectonic models for accretion of the Central Asian Orogenic Belt. *J. Geol. Soc. London*, **164**(1), 31-47.

Wu W., Xu S., Yang J., Yin H., Lu H. and Zhang K. (2010) Isotopic characteristics of river sediments on the Tibetan Plateau. *Chem. Geol.* **269**(3-4), 406-413.

Xiang D., Zhang Z., Xiao W., Zhu W., Zheng D., Li G., Zheng B., Song S., Han C. and Pang, J. (2019) Episodic Meso-Cenozoic denudation of Chinese Tianshan: evidence from detrital apatite fission track and zircon U–Pb data, southern Junggar Basin margin, NW China. *J. Asian Earth Sci.* **175**, 199-212.

Xiao W. J., Windley B. F., Chen H. L., Zhang G. C. and Li J. L. (2002) Carboniferous-Triassic subduction and accretion in the western Kunlun, China: Implications for the collisional and accretionary tectonics of the northern Tibetan Plateau. *Geology* **30**, 295-298.

Yang Y., Fang X., Galy A., Li M., Appel E. and Liu, X. (2014) Paleoclimatic significance of rare earth element record of the calcareous lacustrine sediments from a long core (SG-1) in the western Qaidam Basin, NE Tibetan Plateau. *J. Geochem. Explor.* **145**, 223-232.

Yang Y., Fang X., Li M., Galy A., Koutsodendris A., and Zhang W. (2015). Paleoenvironmental implications of uranium concentrations in lacustrine calcareous clastic-evaporite deposits in the western Qaidam Basin. *Palaeogeogr. Palaeoclimatol. Palaeoecol.* **417**, 422-431.

Yang Y., Galy A., Fang X., Yang R., Zhang W. and Zan J. (2017) Eolian dust forcing of river chemistry on the northeastern Tibetan Plateau since 8 Ma. *Earth Planet. Sci. Lett.* **464**, 200-210.

Ye C., Yang Y., Fang X., Zhang W., Song C., and Yang R. (2020). Paleolake salinity evolution in the Qaidam Basin (NE Tibetan Plateau) between~ 42 and 29 Ma: Links to global cooling and Paratethys sea incursions. *Sediment. Geol.* **409**, 105778.

Yin, A. and Harrison, T. M. (2000) Geologic evolution of the Himalayan-Tibetan orogen: *Annu. Rev. Earth Planet. Sci.* **28**, 211-280.

Yuan W., Carter A., Dong J., Bao Z., An Y. and Guo Z. (2006) Mesozoic-Tertiary exhumation history of the Altai Mountains, northern Xinjiang, China: new constraints from apatite fission track data. *Tectonophysics* **412**(3-4), 183-193.

Zachos J., Pagani M., Sloan L., Thomas E. and Billups K. (2001) Trends, rhythms, and aberrations in global climate 65 Ma to present. *Science* **292**(5517), 686-693.

Zhai Y., and T. Cai (1984) The Tertiary system of Gansu province. In *Gansu Geology*. People's Press of Gansu, China. pp. 1-40,

Zhang W., Chen J., Ji J. and Li G. (2016) Evolving flux of Asian dust in the North Pacific Ocean since the late Oligocene. *Aeolian Res.* **23**, 11-20.

Zhao W., Sun Y., Balsam W., Lu H., Liu L., Chen J. and Ji, J. (2014) Hf-Nd isotopic variability in mineral dust from Chinese and Mongolian deserts: implications for sources and dispersal. *Sci. Rep.* **4**, 5837.

Zhao W., Sun Y., Balsam W., Zeng L., Lu H., Otgonbayar K. and Ji, J. (2015) Clay-sized Hf-Nd-Sr isotopic composition of Mongolian dust as a fingerprint for regional to hemispherical transport. *Geophys. Res. Lett.* **42**(13), 5661-5669.

Zhuang G., Zhang, Y. G., Hourigan J., Ritts B., Hren M., Hou M., Wu M. and Kim B. (2019) Microbial and geochronologic constraints on the Neogene paleotopography of northern Tibetan Plateau. *Geophys. Res. Lett.* **46**(3), 1312-1319.

Ziegler C. L., Murray, R. W., Hovan, S. A. and Rea D. K. (2007) Resolving eolian, volcanogenic, and authigenic components in pelagic sediment from the Pacific Ocean. *Earth Planet. Sci. Lett.* **254**(3-4), 416-432.

FIGURE CAPTIONS

Figure 1. Map of the study areas. **(a)** Map of central and eastern Asia, showing the modern, simplified dust storm tracks and near-surface wind patterns (red arrows) and the hypothetical "glacial" dust storm tracks (blue arrows) to the Chinese Loess Plateau (CLP) (redrawn from Licht et al., 2016) with the locations of the Linxia and Xining (this study) and Tianshui Basins (Chen and Li, 2013). **(b)** Structural map of the Longzhong Basin on the northeastern Tibetan Plateau (redrawn from Dai et al. 2006). Geological map of the Xining Basin **(c)** and Linxia Basin **(d)**, showing the surrounding mountains, major structures, and yellow star indicating the locations of the studied XJ and HLD sections (redrawn from Dai et al., 2006, and Fan et al., 2006).

Figure 2. Depth profile of the Nd isotopic variations along the HLD section from the Linxia Basin (lithology and magnetostratigraphy are redrawn from Fang et al., 2016)

Figure 3. Depth profile of the Nd isotopic variations along the XJ section from the Xining Basin (lithology and magnetostratigraphy are redrawn from Dai et al., 2006).

Figure 4. Nd isotopic compositions expressed in $\varepsilon_{Nd}(0)$ values of the bulk versus the clay-sized (<2 μm) fraction. (**a**) HLD section in the Linxia Basin and (**b**) XJ section in the Xining Basin.

Figure 5. Map showing the modern distribution of Nd isotopic compositions expressed in $\varepsilon_{Nd}(0)$ values for various surface sediments in northern China and Mongolia. (**a**) Map showing Asian dust source areas and the GPC3 borehole in the North Pacific Ocean. (**b**) Zoomed-in map of the dashed black rectangle in (**a**). The two enlarged maps show the Nd isotopic distribution around the Qaidam Basin (**c**) and the Xining Basin (**d**). Note that the dots with black outlines are from this study; other data are from surface sediments (desert, fluvial, moraine, and loess samples) and soils (Blayney et al., 2019; Chang et al., 2010; Chen et al., 2007; Clift et al., 2017; Garzione et al., 2005; He et al., 2019; Li et al., 2009; Liu et al., 1994; Nakano et al., 2004; Rao et al., 2015; Wu et al., 2010; Zhao et al., 2014, 2015).

Figure 6. Cenozoic variations in the $\varepsilon_{Nd}(0)$ values in the NTP. (**a**) Linxia Basin. (**b**) Xining Basin. (**c**) Tarim Basin. The bulk sediment data for the MG and WJS sections are close to the depocenter of the Linxia Basin (Garzione et al., 2005). The bulk data of the HLD section for the period 12-5 Ma are from Yang et al. (2017). The data from the Tianshui Basin are the bulk and 28-45 μm fraction of the Qin'an eolian section from Chen and Li (2013). The bulk sediment data of the XG-TS section from the Xining Basin are from He et al. (2019). The bulk sediment data of the Aertashi section from the Tarim Basin are from Blayney et al. (2019). The NPO dust data are presented for comparison and are from core GPC3 (Pettke et al., 2002; Zhang et al., 2016).

Figure 7. The reconstructed Cenozoic eolian dust Nd isotopic variations (expressed in $\varepsilon_{Nd}(0)$ values) in the NTP and their comparison with other records. (**a**) Dust $\varepsilon_{Nd}(0)$ values in the NTP and core GPC3. For the NTP, the bold orange curve represents the locally weighted scatterplot smoothing (LOWESS, smoothing factor is 0.15) fitting of the NTP dust data from the Nd isotopic compositions of the <2 μm fraction in the Linxia and Xining Basins, and the green curve represents the uncertainty envelope (note that the two very negative data with dashed circles at 30-36 Ma have been excluded for the composite curve). (**b**) The NTP contributions to the NPO dust estimated by mass balance by equation (1) between NTP and NPO records and assuming a constant CAOB Nd composition in various scenarios (CAOB ε_{Nd} values of -1, -3, -7, and -5.5). The black line denotes the NTP contribution estimated by the ε_{Nd} mean value of -5.5 for the <2 μm fraction of the CAOB surface sediments (Table S3). The yellow shaded area shows the uncertainty envelope of varying Nd concentrations (1σ change in Nd mean concentration of <2 μm fraction of the CAOB surface sediments, from 24 to 46 μg/g, Table S3) corresponding to CAOB ε_{Nd} values of -5.5. The CAOB contribution of the western Tarim Basin (for the period between 38 and 30 Ma) to NPO dust is shown by the light blue area. Two sensitivity tests for the Tarim Basin contribution before 25 Ma are shown in the bold blue (Tarim Basin represents 100% of the NTP contribution) and violet lines (Tarim Basin represents 50% of the NTP contribution). (**c**) Convergence rates between India and Eurasia (Lee and Lawver, 1995; Molnar and Stock, 2009; van Hinsbergen et al., 2011). (**d**) Offset in the $\varepsilon_{Nd}(0)$ values between the bulk sediment and the <2 μm fraction in the XJ section of the Xining Basin. (**e**) Tectonic subsidence depth in the Aertashi section in the western Tarim Basin (Blayney et al., 2019). (**f**) Average uplift (blue line) and subsidence (green line) rates in the southern Tarim Basin (Jiang and Li, 2014). (**g**) Sediment accumulation rate in central Asia

(Métivier et al., 1999). **(h)** The onset of eolian sediment development (orange arrows) in central Asia (Sun et al., 2010; Zheng et al., 2015) and in the CLP (Guo et al., 2002; Qiang et al., 2001). (**i**) Eolian mass accumulation rate (MAR) at ODP site 1208 (Zhang et al., 2016) and in core GPC3 (Janecek and Rea, 1983). To show the variations in the two records on the same graph, the GPC3 data have been blown up 50 times. The vertical gray bars mark the two transition periods of ~42 Ma and ~25 Ma.

Figure 8 Schematic diagram of Asian dust production and transport from the NTP and CAOB regions to the proximal CLP, the distal North Pacific and even Greenland. (**a**) The Neogene-Quaternary regime (modified after Chen and Li, 2011 with tectonically active NTP and CAOB regions in combination with a strong East Asian monsoon system). (**b**) The regime prior to the late Oligocene (further modified from (**a**) with high elevations in south-central Tibet but a less tectonically active NTP and a relatively low-relief CAOB).

Declaration of interests

☒ The authors declare that they have no known competing financial interests or personal relationships that could have appeared to influence the work reported in this paper.

☐The authors declare the following financial interests/personal relationships which may be considered as potential competing interests: